Available online at www.sciencedirect.com
ScienceDirect
Trans. Nonferrous Met. Soc. China 34(2024) 203−218
Transactions of Nonferrous Metals Society of China
www.tnmsc.cn

High-temperature oxidation behaviors and mechanical properties of TiAlCrMn HEAs during heat treatment

Ping-hu CHEN[1], Bai-chun LI[2], Zhen LIU[1], Ying-hao ZHOU[3], Rui-qing LI[4], Yun ZHANG[5]

1. Additive Manufacturing Institute, College of Mechatronics & Control Engineering, Shenzhen University, Shenzhen 518060, China;
2. School of Materials Science and Engineering, Harbin Institute of Technology (Shenzhen), Shenzhen 518055, China;
3. Department of Mechanical Engineering, City University of Hong Kong, Hong Kong, China;
4. State Key Laboratory of High Performance Complex Manufacturing, Light alloys Research Institute, Central South University, Changsha 410083, China;
5. School of Mechanical Engineering, Hunan University of Science and Technology, Xiangtan 411201, China

Received 22 June 2022; accepted 3 November 2022

Abstract: A series of TiAlCrMn high entropy alloys (HEAs) with variable atomic ratios of Al, Cr, and Mn were prepared using vacuum melting. High-temperature oxidation behaviors and mechanical properties were investigated before and after heat treatment. The oxidation mass gain rate is declined dramatically with increasing Al, Cr, and Mn element contents. Enhanced oxidation resistance is attributed to a continuously dense (Al,Cr)-rich oxidation layer, which can hinder the inter-diffusion of O and alloying elements. Furthermore, microhardness increases monotonously with increasing Al, Cr, and Mn element contents of the alloys before and after heat treatment. Grain coarsening can result in lower microhardness, but precipitation strengthening contributes to higher hardness of the alloys with high alloying element contents. Meanwhile, deformation-induced strengthening also contributes to higher compressive strength. The value after heat treatment at 500 °C is lower than that of as-cast samples while an increased value occurs after heat treatment at 900 °C accompanied by sacrificing the malleability.

Key words: high entropy alloys (HEAs); oxidation resistance; microstructural evolution; microhardness; compressive strength

1 Introduction

Ti and its alloys have been extensively used in the aerospace industry owing to some advantages of low density, high specific strength, and excellent thermal resistance, etc [1−3]. For as-cast Ti alloys, suitable heat treatment could be an essential processing approach to adjust the microstructure and improve engineering component properties before the engineering application [4−6]. Nevertheless, creep resistance and fatigue property could be deteriorated severely as a result of weak high-temperature oxidation resistance during high temperature heat treatment, thus resulting in structural failure, and even generating a significant economic loss [7−9]. Vacuum or atmospherically protected heat treatment could be carried out to lessen the influence of high-temperature oxidation on the properties of Ti-based engineering components, but this could cause a huge excess charge [10−13].

Due to their stable solid solution structure, severe lattice distortion, and sluggish diffusion effects, high-entropy alloys (HEAs) exhibit better thermal stability [14]. HEAs could be a class of

Corresponding author: Yun ZHANG, Tel: +86-15116337996, E-mail: yun_zhang66@163.com
DOI: 10.1016/S1003-6326(23)66392-7

potential structural and functional material in the future [15]. Especially, high strength steel with high density could be substituted by light-weight HEAs with remarkably high-temperature mechanical properties, which could be applied within a wide temperature range, in order to promote flight capabilities in the aerospace field [16]. For this purpose, many researchers also studied how alloying excellent oxidation resistance elements (such as Al, Cr, Si, Nb, or Zr) could be added to improve high-temperature oxidation resistance of the designed materials with overcoming strength−plastisity trade-off. An amorphous TiNiSiCrCoAl HEA coating was fabricated on the surface of Ti−6Al−4V to improve high-temperature oxidation resistance at 800 °C. The results indicated that the presence of TiO_2 within the σ phase prevented the formation of a continuously dense Al_2O_3 protective layer. But excellent oxidation resistance occurred in the amorphous phase with Cr and Si elements [8]. The influence of Al and Si elements on high-temperature oxidation resistance was also studied by KNAISLOVÁ et al [17]. They found that higher-content Si could contribute to the most resistance to the internal stress of the oxidation layer, increase the layer's adherence and promote the formation of a compact Al_2O_3 protective layer for TiAl alloys [18]. Similar to this, a continuously compact Al_2O_3 protective layer could contribute to inhibiting the diffusion of an oxygen atom into the oxide layer [19]. In addition, Cr, Nb, and Ta elements could encourage the formation of protective $(Al_xCr_{1-x})_2O_3$ at 700−1000 °C and enhance high-temperature oxidation resistance without sacrificing mechanical properties. Meanwhile, the oxidation mechanism was discussed in Refs. [20−22]. Nonetheless, the aforementioned research had not reported high-temperature oxidation resistance of high-content Mn, Al, and Cr co-alloyed Ti alloys.

In this work, a series of $Ti_{1-3x}Al_xCr_xMn_x$ (x=5, 10, 15, and 20, at.%) HEAs were prepared by vacuum melting. Heat treatments were performed to tailor microstructure and mechanical properties. Besides, high-temperature oxidation resistance of $Ti_{1-3x}Al_xCr_xMn_x$ HEAs was studied during heat treatment at 500 and 900 °C. The oxidation mechanism was discussed in detail. Meanwhile, mechanical properties were explored after heat treatment. These works can provide fundamental guidance for the development of novel materials and the formulation of heat treatment processes in the future.

2 Experimental

2.1 Materials and preparation of samples

A series of $Ti_{1-3x}Al_xCr_xMn_x$ (x=5, 10, 15, and 20, at.%) HEAs were fabricated using a vacuum melting furnace with a mold of 10 mm × 10 mm × 70 mm. Four different materials were named as T5-AC (x=5), T10-AC (x=10), T15-AC (x=15), and T20-AC (x=20). All samples with dimensions of 10 mm × 10 mm × 5 mm were cut to carry out the oxidation testing and hardness measurement. Meanwhile, the samples for compressive testing were cut to a size of 3 mm × 3 mm × 5 mm. Each sample was ground using 400, 800, 1200, 1500, and 2000 grit sandpapers, and followed by cleaning and drying.

2.2 Heat treatment

Heat treatment was carried out in the muffle furnace at 500 and 900 °C in the atmospheric environment. The detailed steps were as follows. Firstly, the furnace temperature was increased gradually from room temperature to 500 or 900 °C at a constant speed of 30 °C/min. Secondly, the test samples were placed into the muffle furnace after the stability of furnace temperature at 500 or 900 °C, maintained for 60 min, and then cooled in air. After heat treatment, the samples were named as T5-5 (500 °C), T5-9 (900 °C), T10-5 (500 °C), T10-9 (900 °C), T15-5 (500 °C), T15-9 (900 °C), T20-5 (500 °C) and T20-9 (900 °C).

2.3 Oxidation test

An electronic weighing balance with an accuracy of 0.1 mg was employed to record the mass of samples before heat treatment. Afterward, the mass of samples after heat treatment at 500 or 900 °C was recorded, and the oxidation mass gain rate was calculated using the equation of $v=(m_f-m_s)/t$, where v was the oxidation mass gain rate, g/m^2; m_s and m_f represented the masses of the samples before/after oxidation, g; t was the oxidation time, min.

2.4 Mechanical properties testing

The digital micro Vickers hardness tester was employed to measure the microhardness of

$Ti_{1-3x}Al_xCr_xMn_x$ (x=5, 10, 15, and 20, at.%) HEAs before/after heat treatment under a load of 4.9 N with a duration time of 15 s. Five points were measured for each sample. Their average value was considered as the final value. In addition, a universal testing machine was employed to obtain the relationship curves between the compressive stress and strain at a crosshead speed of 0.3 mm/min. At least three measurements were taken for each sample to calculate an average value as the final value.

2.5 Material characterization

High-energy X-ray diffraction (HE-XRD, D8 discover, Bruker, Germany) was applied to analyze the phase of different samples. XRD was operated at 40 kV and 70 mA using a scanning speed of 2 (°)/min over a range of 2θ=30°−120°. Scanning electron microscope (SEM, TESCAN MIRA 3 LMH/LMU, Czech Republic) was employed to characterize the micromorphology of the surface and cross-section. Furthermore, the corresponding elemental distribution of the oxidation layer was analyzed by EDS. In order to further explore the correlation of heat treatment, microstructure, and mechanical properties, electron back-scattered diffraction (EBSD, FE-SEM, Carl Zeiss, SUPRA®55) was employed. For EBSD analysis, samples were ground with 400, 800, 1200, 2000, 5000, and 7000 SiC grit papers before being mechanically polished by diamond suspension with the size of 3 μm. Afterward, vibratory polishing was carried out using diamond suspension with a grain size of 20 nm for 5 h. EBSD was employed by an accelerating voltage of 20 kV with a scanning step size of 50 nm to obtain the relevant information, such as grain size, texture, inverse pole figure (IPF), pole figure (PF), etc.

3 Results and discussion

3.1 Initial microstructure

Figure 1 shows angle-selected backscattering (AsB) images and EDS results of as-cast TiAlCrMn system HEAs. The second phase and grain boundary do not appear obviously in the T5-AC and T10-AC samples. But obvious grain boundary exists in the T15-AC sample with a grain size of 100 μm. Meanwhile, a small amount of the second phase is precipitated near the grain boundary. These second phases are measured between 2 and 10 μm in length and below 1 μm in width, as shown in Fig. 1(c). More specifically, dual-phases are discovered in the T20-AC sample. These dual phases with alternate bands are discovered within a single grain. In light of EDS results, Cr and Mn elements are enriched in the second phase with a low content of Al when a relatively small deviation occurs in the T5 and T10 samples, as shown in Fig. 1(e).

Meanwhile, HE-XRD patterns are shown in Fig. 2 to further analyze their phases. These results indicate that a dual hcp structure with increasing Al, Cr, and Mn elements can be formed gradually by transferring phase from a single bcc structure. Consequently, more Ti atoms can be replaced by other atoms, progressively causing the lattice constants of bcc structure to shrink from 0.321 nm

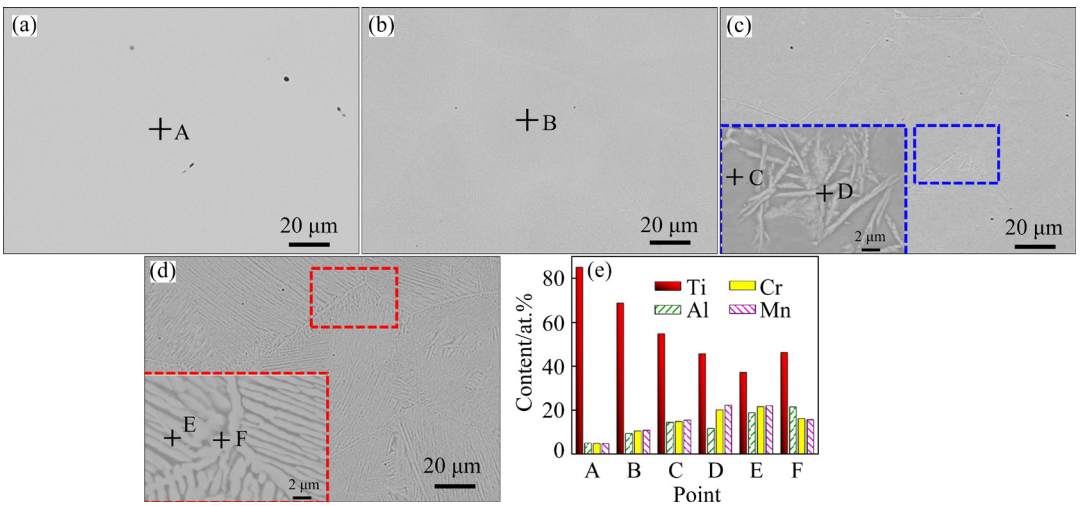

Fig. 1 AsB images (a−d) and EDS elemental distribution (e) of as-fabricated Ti−Al−Cr−Mn system HEAs: (a) T5-AC; (b) T10-AC; (c) T15-AC; (d) T20-AC

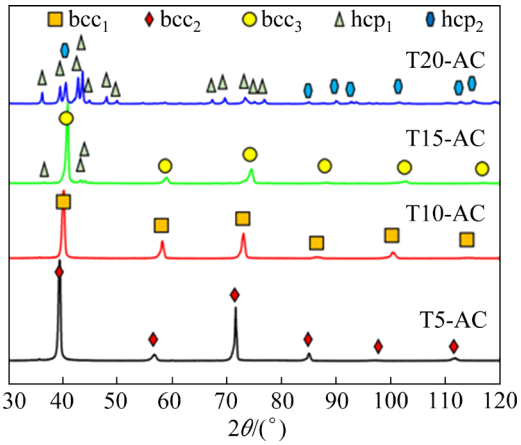

Fig. 2 HE-XRD patterns of samples

of T5-AC sample to 0.312 nm of T15-AC sample. It is well known that the evolution of microstructure can affect the mechanical properties and high-temperature oxidation resistance.

3.2 High-temperature oxidation behaviors

Figure 3 shows the oxidation mass gain rate of TiAlCrMn HEAs after heat-treatment at 500 and 900 °C with a duration time of 60 min. The oxidation mass gain rate of the samples after heat treatment at 500 °C can be changed indistinctively with the change of surface color, as shown in Fig. 3. But when the heat treatment temperature reaches 900 °C, the oxidation mass gain rate of T5 sample is greater than 66 g/m^2, and it decreases gradually with increasing the Al, Cr and Mn element contents. Compared with the T5 sample, the oxidation mass gain rates of T10, T15, and T20 samples are decreased respectively by 65.2%, 84.6%, and 89.8%. In terms of macro-/micro-structure, the oxidation layer of T5 is peeled completely off during air cooling when the exfoliation phenomenon of the oxidation layer in the T10, T15, and T20 samples never occurs during air cooling. But a small amount of oxide for the T10 sample can be peeled off after a while. It is indicated that high-temperature oxidation resistance can be improved gradually with increasing Al, Cr, and Mn element contents. Meanwhile, the resistance to cracking and peeling can be dramatically enhanced during the rapid cooling process.

An excellent oxidation resistance can be attributed to the formation of a continuously compact oxide with excellent oxidation resistance, such as Al_2O_3, Cr_2O_3 and SiO_2. Figure 4 shows HE-XRD patterns of the oxidation layer on the surface of the samples. A large amount of rutile TiO_2 with a small amount of α-Al_2O_3, MnO_2, and their composite oxides are found in the T5 sample. But Al_2O_3, and Cr_2O_3 protective oxides, and bcc-structure matrix phase exist in the subsurface of the T5 sample. In addition, more Cr-O, and Al_2O_3 oxides are shown in the T15 and T20 samples. As shown in Fig. 5, there is a significant change in the microstructure of oxidation layer. Columnar oxides and quasi-symmetrically blocky oxides are discovered on the oxidation layer of T5 sample. And more finely columnar oxide also appears in the T10 sample without blocky oxide. However, some islands with blocky oxides are surrounded by nanoscale columnar oxides in the T15 sample. These blocky oxides are relatively continuous without high compactness. The T20 sample, however, differs due to its denser blocky oxidation layer. Furthermore, in order to explore further

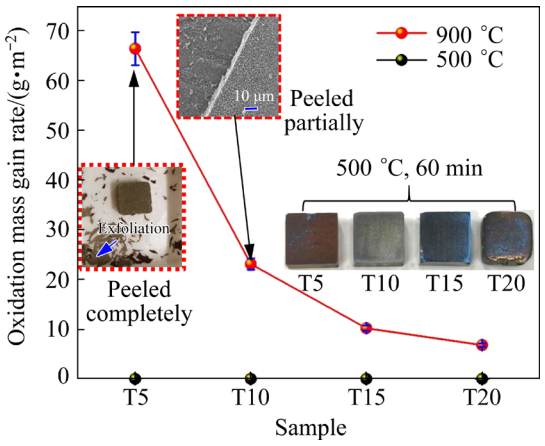

Fig. 3 Oxidation mass gain rate of TiAlCrMn HEAs after heat treatment

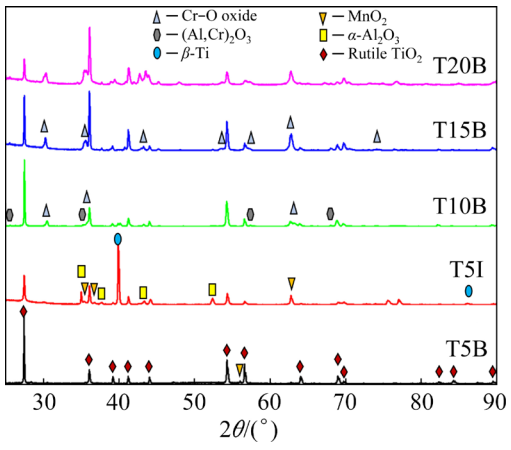

Fig. 4 HE-XRD patterns of TiAlCrMn HEAs after heat treatment

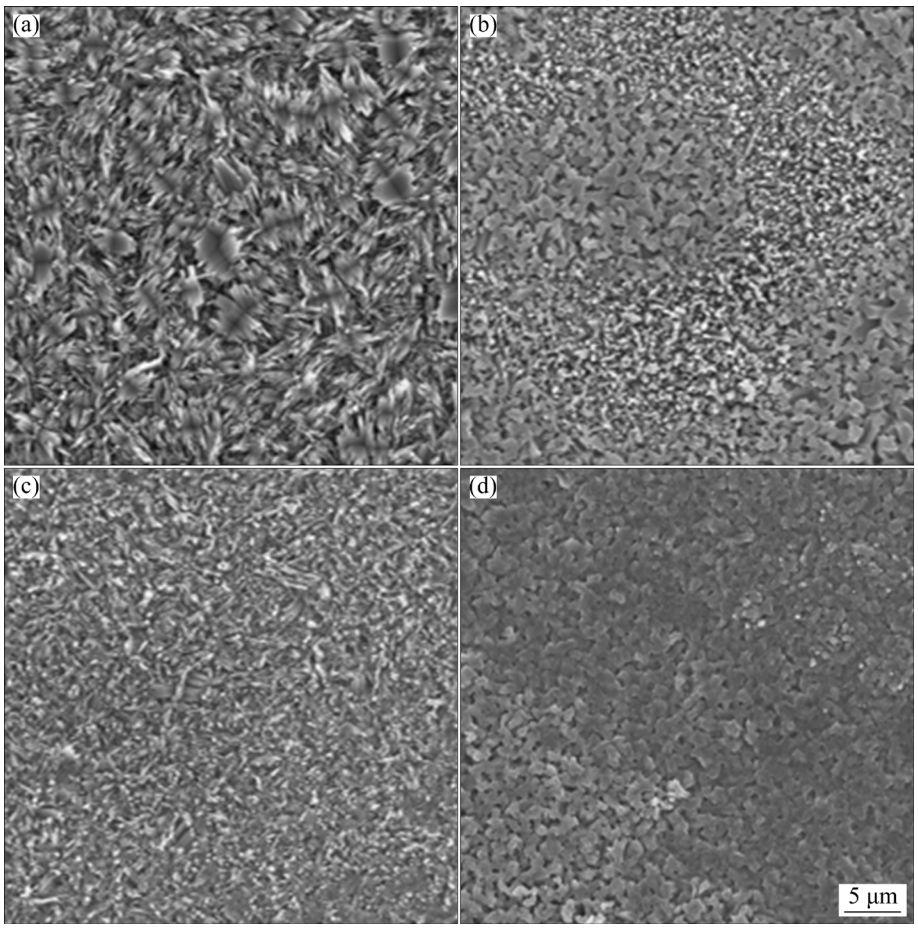

Fig. 5 High-temperature oxidation characteristics of TiAlCrMn HEAs after heat treatment at 900 °C: (a) T5; (b) T10; (c) T15; (d) T20

cracking and peeling behaviors of the oxidation layer, micromorphologies of the top surface and section surface are shown in Fig. 6. The oxide grows from the inside to the outside in a non-uniform direction. Columnar oxides (nano-/sub micro-scale) are smaller than quasi-symmetrically blocky oxides (about 5 μm). Meanwhile, obvious subsurface morphologies after peeling are discovered in Figs. 6(d−f). A large number of channels are formed owing to the irregular breakup caused by the nonuniform distribution of the oxides. In terms of the corresponding ESD results in Table 1, the oxides of the top surface include mainly Ti, Al, and Mn for Points P1 and P2 in Figs. 6(b, c). But higher-content of Cr appears in the fracture surface of the oxidation layer, as demonstrated in Figs. 6(e, f). For Point P6, the Cr content reaches 24.9% in the total atomic fraction of all alloying elements excluding O element.

Combined with the similar morphologies at the cross section of four samples (Fig. 7), the oxidation layer in the T5 sample is not visible on account of fully peeling during air cooling. However, O is still captured in the near-surface of the matrix. It is noted that O not only permeates into the oxidation layer, but also permeates across the oxidation layer to the matrix. An obvious oxidation layer is discovered in the T10, T15, and T20 samples. Further, the thickness of the oxidation layer decreases rapidly with increasing the Al, Cr, and Mn element contents. The thickness of the oxidation layer in the T10 sample is about 72 μm while that of the T15 and T20 samples is 11.4 μm and below 3 μm, respectively. However, due to thermal stress caused by cooling and sample preparation, cracks still exist in the oxidation layer of the T10 sample. The oxidation layer can be divided into four zones: outer loose layer, middle granular layer, inner compact layer, and permeability layer. Middle granular layer is a discontinuous oxide and enclosed by finer oxide. For this reason, the oxidation layer is not peeled off

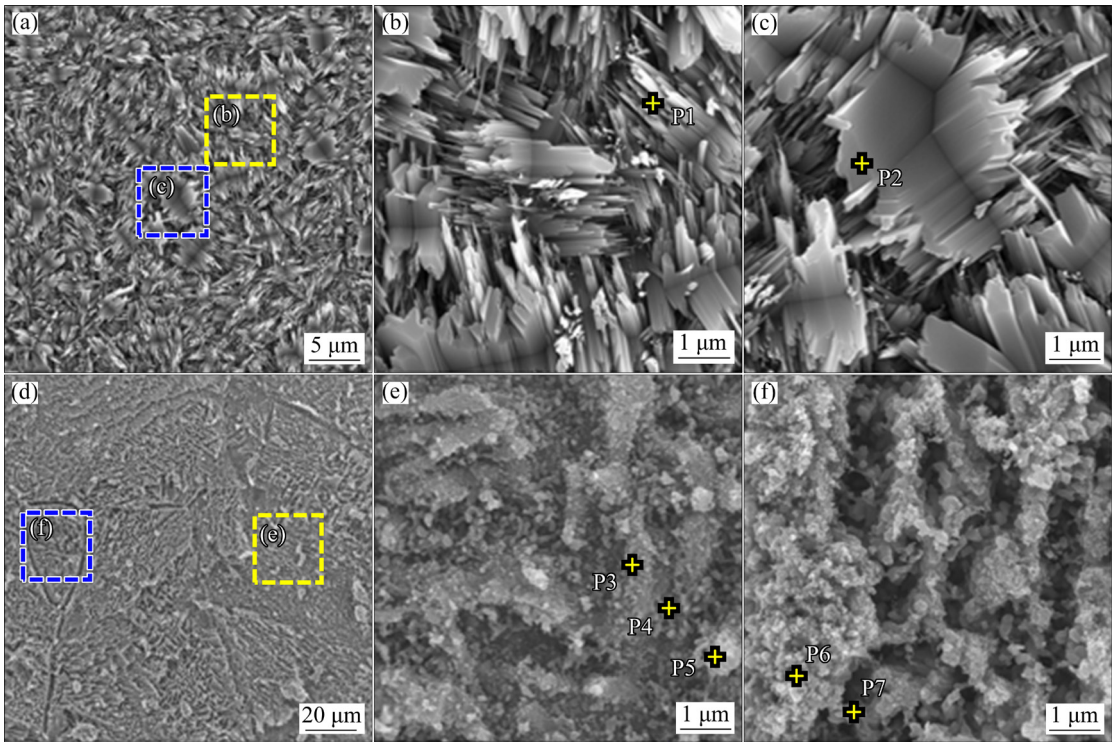

Fig. 6 Surface (a−c) and sub-surface (d−f) morphologies of T5 sample

Table 1 Contents of elements for Points P1−P7 in Fig. 6 (at.%)

Element	P1	P2	P3	P4	P5	P6	P7
O	69.59	79.01	61.4	74.61	67.1	52.5	69.47
Ti	26.21	18.71	32.07	19.79	28.6	18.67	27.1
Al	2.83	1.75	1.4	0.49	0.8	0.97	0.33
Cr	0.05	0.01	4.44	4.13	2.39	6.84	2.47
Mn	1.33	0.52	0.7	0.98	1.11	1.01	0.63

because part of the thermal stress is released adequately during air cooling. In the light of the corresponding EDS elemental distribution in line scanning, Mn-rich, and Al-rich oxide, in addition to Ti oxide, make up the majority of the outer loose layer. And the middle granular layer has a large amount of Ti oxide and minimal Al and Mn-rich oxides. But a relatively dense Al_2O_3 is present in the inner compact layer when Cr-rich oxide with a thickness of 2−4 μm is discovered in the permeability layer. Compared to the T5 and T10 samples, a large amount of Cr-rich and Al-rich protective oxides are embedded into the porosity of Ti oxides in the T15 and T20 samples. Furthermore, a continuously dense oxidation layer is formed to inhibit the formation of new oxides owing to the diffusion of O element.

The aforementioned results can be attributed to a synergistic effect of microstructure and the release of internal stress. For T5, relatively porous rutile TiO_2 (R-TiO_2) is a major oxide in the oxidation layer owing to 85 at.% Ti and lower Gibbs energy of R-TiO_2 in T5 sample, as shown in Figs. 6(a−c) and Table 1. The atomic ratios of Ti, Al, Cr, and Mn elements are 86.2%, 9.3%, 0.1%, and 4.4%, respectively. O atom can permeate to the interface via these pores. With increasing oxidation time, MnO_2, Cr_2O_3, and Al_2O_3 can then be formed in the sub-surface or the interface, as shown in Fig. 4. A large number of Cr-rich oxides can be discovered with a range of 7.3%−24.9% Cr content. Although Cr_2O_3 and Al_2O_3 are protective oxides, a continuously dense oxidation layer is not formed owing to low content. Afterward, O can diffuse freely from the surface to the interface. During the rapid growth process of the oxides, growth stress can be formed owing to different Pilling−Bedworth ratio (PBR) of the oxides during the isothermal oxidation process [23−25]. New oxides are formed inside the oxidation layer, thus resulting in its expansion and the initiation of cracks. However, the addition of Cr causes an increase in activity ratio of a(Al)/a(Ti) (a represents thermodynamic activity of alloying elements), which promotes the

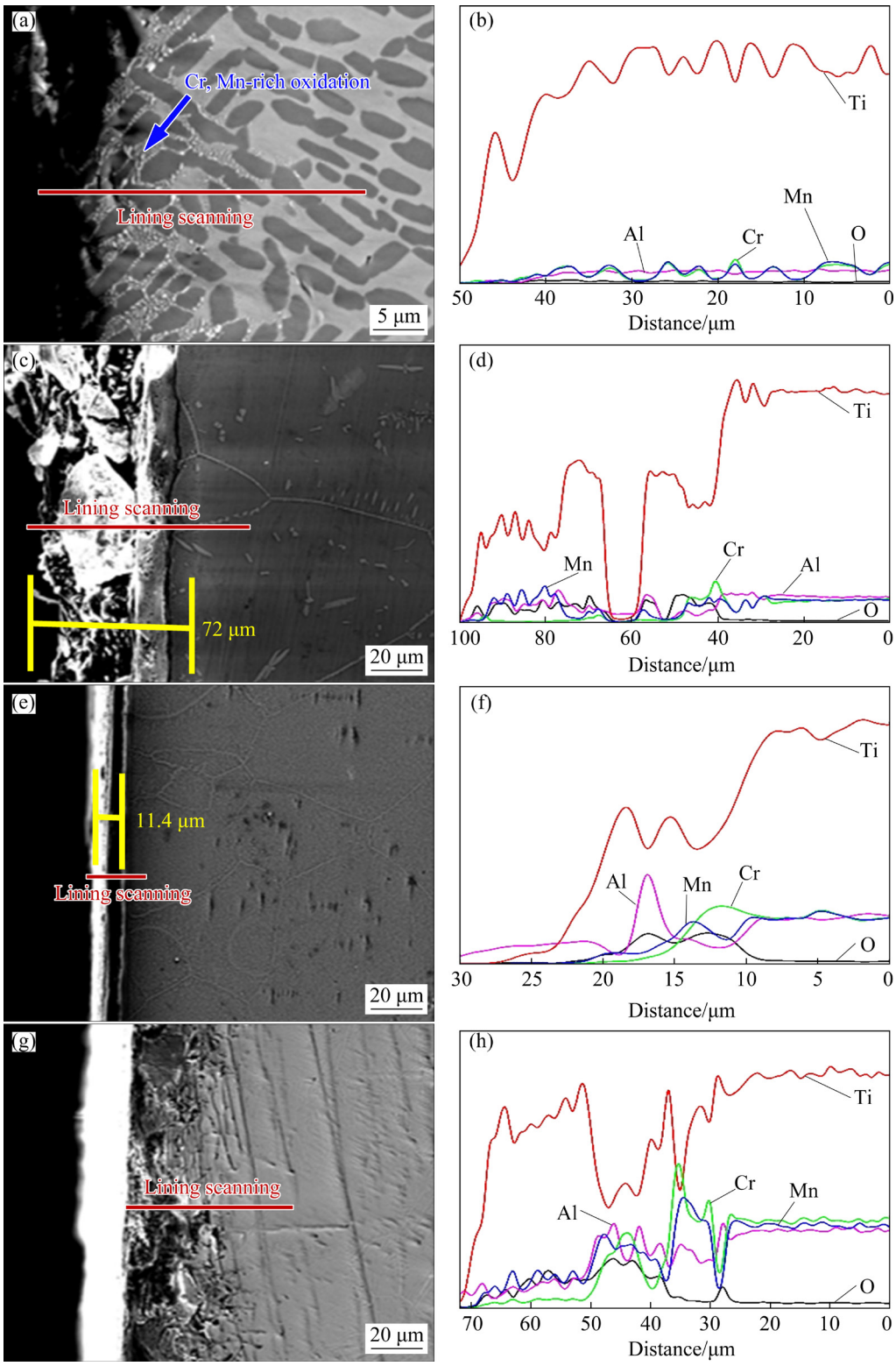

Fig. 7 Cross-section morphologies (a, c, e, g) and elemental distributions (b, d, f, h) of oxidation layers after heat treatment at 900 °C: (a, b) T5-9; (c, d) T10-9; (e, f) T15-9; (g, h) T20-9

formation of Al_2O_3 and results in poor oxygen permeability [26−28]. Besides, the oxidation process can be prevented when the Cr content is above a critical value of 10 at.%. Conversely, oxidation cannot be inhibited if the Cr content is too low [29−31]. The value of a(Al)/a(Ti) is only 0.059. As a result, Al_2O_3 oxide with continuous and compact structure cannot be formed on the surface

of T5 sample. With the increase of Al, Cr and Mn element content, a(Al)/a(Ti) can reach a larger value from 5.9% to 50%. Therefore, O can be inhibited from penetrating further into the matrix, and a continuously dense Al_2O_3 oxide is formed to obtain excellent oxidation resistance in the T20 sample. In addition, the temperature gradient is large during air cooling from 900 °C to room temperature at a rapid rate, resulting in high thermal stress. The exfoliation can also occur due to the different coefficients of linear expansion for different oxides caused by the release of thermal stress without adequate time. In addition, it was also reported [32] that Al_2O_3 can be formed preferentially due to the fact that the order of metal reducibility is Al>Ti>Cr, and the thermal expansion coefficients of R-TiO_2 and α-Al_2O_3 coatings are about 7.3×10^{-6} and 9.2×10^{-6} K^{-1}, respectively [33].

3.3 Microstructural evolution and its influence on mechanical properties

Figure 8 indicates that AsB morphologies of TiAlCrMn HEAs after heat treatment of 500 °C are highly consistent with those of as-cast samples, which proves that the microstructure of the samples is extremely stable below 500 °C. Nevertheless, heat treatment at 900 °C significantly alters the microstructure of samples. As shown in Fig. 9, a large amount of second phase precipitates dispersedly in the T5-9 sample, and the alloying elements are re-assigned into two phases. Cr and Mn elements are enriched in the Region 1 while Ti is enriched in the Region 2. The contents of elements are given in Table 2. For T10-9 sample, second phases with enriched Cr and Mn are continuously precipitated on or near the grain boundary. However, the nanoscale second-phase particles can be distributed uniformly within the grain, as shown in Fig. 9(c). The crisscross texture is discovered in the T20-9 sample. This microstructural evolution before/after heat treatment can contribute to different mechanical properties.

Figure 10 shows Vickers hardness of the initial and heat treated samples. The values are increased gradually with increasing the Al, Cr, and Mn element contents of the initial and heat treated samples. The microhardness of the T5-AC sample is only $HV_{0.5}$ 307.2. And it is increased for the T10-AC, T15-AC, and T20-AC samples when compared to the T5-AC sample by 32%, 82%, and

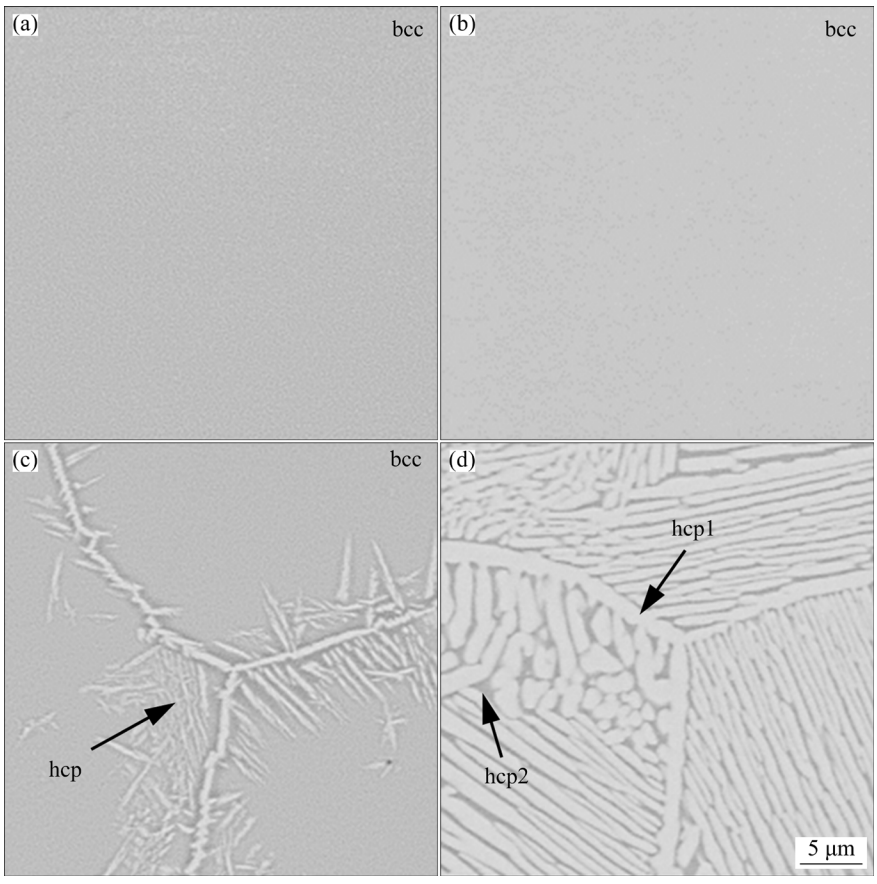

Fig. 8 SEM images of TiAlCrMn HEAs after heat treatment at 500 °C: (a) T5-5; (b) T10-5; (c) T15-5; (d) T20-5

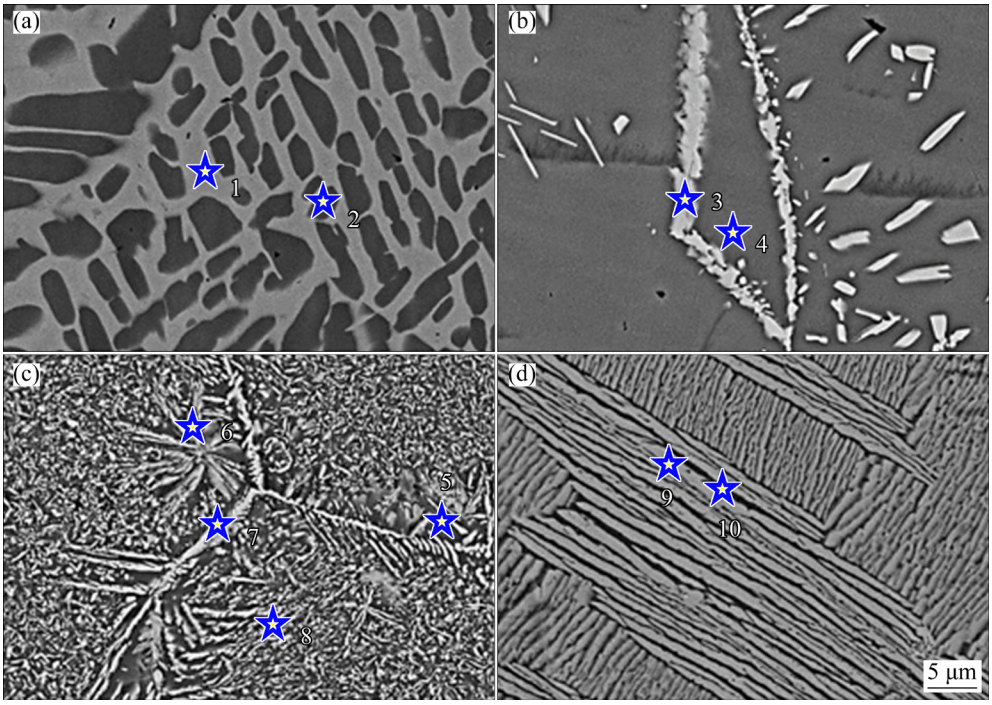

Fig. 9 SEM images of TiAlCrMn HEAs after heat treatment at 900 °C: (a) T5-9; (b) T10-9; (c) T15-9; (d) T20-9

Table 2 Contents of elements for Points 1−10 in Fig. 9 (at.%)

Point	Ti	Al	Cr	Mn
1	77.8	5	8.8	8.4
2	90.8	5.6	1.8	1.8
3	43	2.4	31	23.6
4	72.4	10.8	7.9	8.9
5	57.6	18.1	11.9	12.4
6	52.7	13.1	17.1	17.1
7	46.5	9.2	22.8	21.7
8	56.5	15	14.5	14
9	36.4	19.1	23	21.5
10	47.4	23.3	15.7	13.6

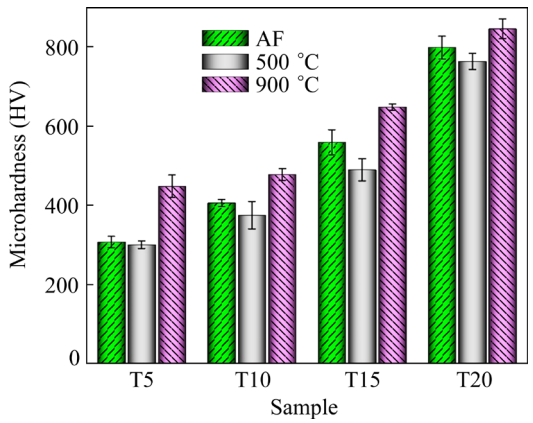

Fig. 10 Microhardness of TiAlCrMn HEAs before/after heat treatment

160%, respectively. A similar trend may be seen in the microhardness of heat treated samples with increasing Al, Cr, and Mn contents. Nevertheless, when greater values are obtained for the samples heat-treated at 900 °C, the microhardness of the samples after heat treatment at 500 °C is lower than that of as-cast samples. It is worth noting that reduced hardness can be attributed only to coarse grains [34,35]. In addition, compressive behavior can be changed owing to microstructural evolution. Just as Fig. 11(a) and Table 3 show, the yield strength of the T5-AC sample is 888.8 MPa, and the compressive strength exceeds 4640 MPa without cracking. This indicates that TiAlCrMn HEAs with a low ratio of alloying elements have excellent plasticity. For the T10-AC sample, yield strength and compressive strength are higher than those of the T5-AC sample, with values of 1260.3 and 6280 MPa, respectively. In light of Figs. 11(a_1, a_2), it is possible for the T10-AC sample to include cracks. But brittle fractures can result in low yield strength and compressive engineering strain. The T15-AC sample has a yield strength of 1618.8 MPa and a compressive strain of 12%. However, the cracking occurs in the T20-AC sample with the compressive strength only of 477.5 MPa. This can be attributed to a synergistic effect between the embrittlement of the material and the solidification

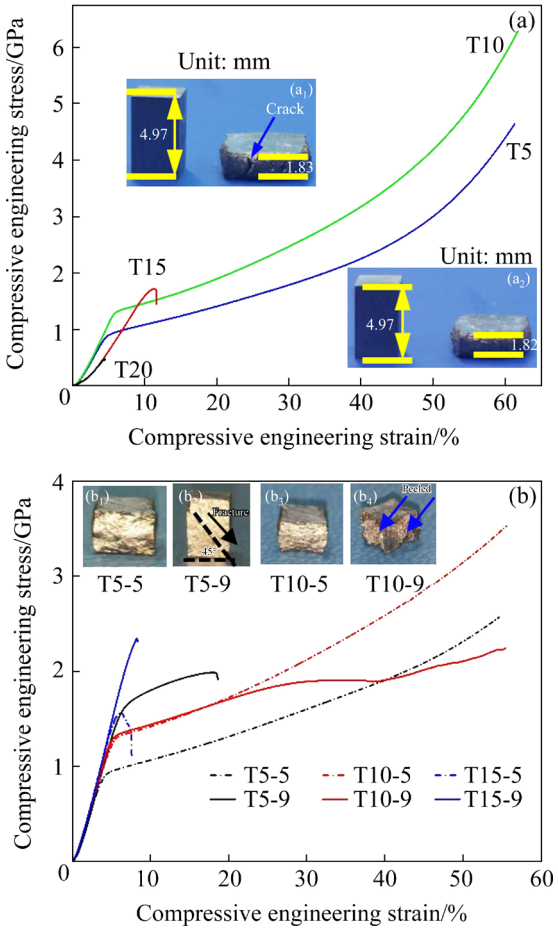

Fig. 11 Compressive stress−strain curves of initial samples (a) and heat treated samples (b)

defects caused by the poor formability of hcp-Ti [36]. As for the yield strength, the values of T10-AC and T15-AC samples are increased by 41.7% and 82.1%, respectively, in comparison to the value of the T5-AC sample. The linear relationship can be indicated with less solidification defects, and by assuming a linear relationship, the yield strength of T20-AC sample can reach 1989.4 MPa.

Table 3 Compressive properties of initial samples

Sample	YS/MPa	UCS/MPa	Compressive strain/%
T5-AC	888.8	4640	63.4
T10-AC	1260.3	6280	63.2
T15-AC	1618.8	1716.3	11.6
T20-AC	–	477.5	4.6

The compressive characteristics of heat-treated samples are displayed in Fig. 12. The increasing rate of compressive strength is in general decreased in a later stage of compression compared with as-cast samples. The yield strength of the T5-5 sample is 5.2% lower than that of the T5-AC sample. And by sacrificing its malleability, the yield strength of the T5-9 sample increases dramatically by 64.1%. From Fig. 12, the compressive strain decreases sharply to 18.6%, and the cracking occurs at 45° to the deformation direction, proving that the crack is initiated by the shear mode [37]. For the initial and heat-treated T10 samples, yield strength has a relatively small fluctuation within the range of ~6%. Nevertheless, the deformability of the T10-5 sample is improved according to Figs. 11(a_2, b_3, b_4). Macro-scale cracks are not discovered on the surface of T10-5 sample, but the exfoliation phenomenon is still present on the surface of T10-9

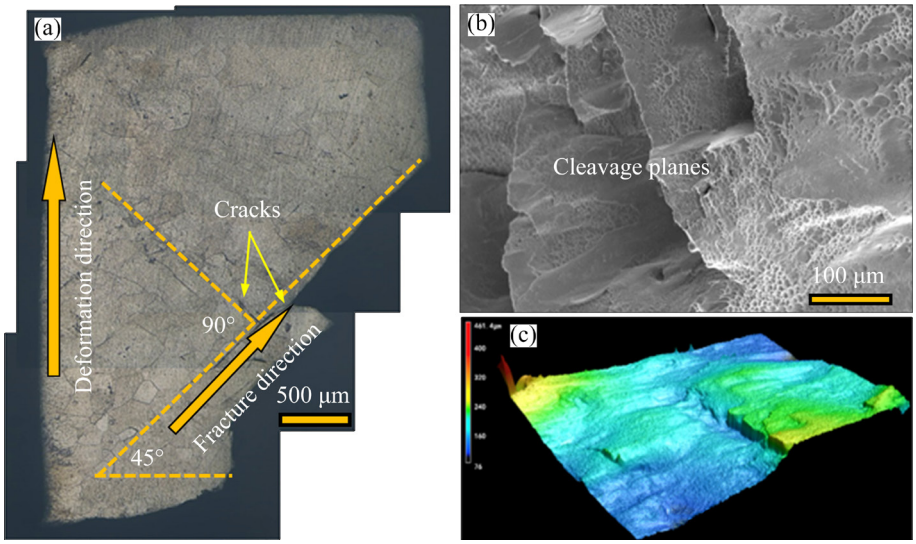

Fig. 12 Compressive morphologies of heat-treated TiAlCrMn HEAs (T5-9 sample): (a) OM image along flank of fracture surface; (b) SEM image of fracture surface; (c) 3D laser confocal image of fracture surface

sample. Hence, engineering stress starts to reduce when the engineering strain reaches 35%, and then increases sequentially after the engineering strain of 40% until the compression experiment is complete. In addition, the same tendency appears in the T15 samples. As compared to the T15-AC sample, the ultimate compressive strength of T15-5 and T15-9 samples is increased by −9.1% and 39.5%, respectively.

The microstructure is heavily influenced by the alloying element [38]. For high-entropy alloys, lattice distortion is caused by a significant variation in atomic diameter among different alloying elements, which results in the formation of a more stable solid-solution structure. In addition, Cr and Mn elements are considered as stabilizing elements of bcc Ti [39], and the Al atom can stabilize the hcp phase [40]. Furthermore, the Mn element also plays a significant role in grain refining [41]. The microstructure of T5-AC and T10-AC samples consists of primary equiaxed grains without texture. But there is a great difference in the size of grains. As shown in Fig. 13, the maximum grain size of T5-AC sample can exceed 200 μm, while that of the

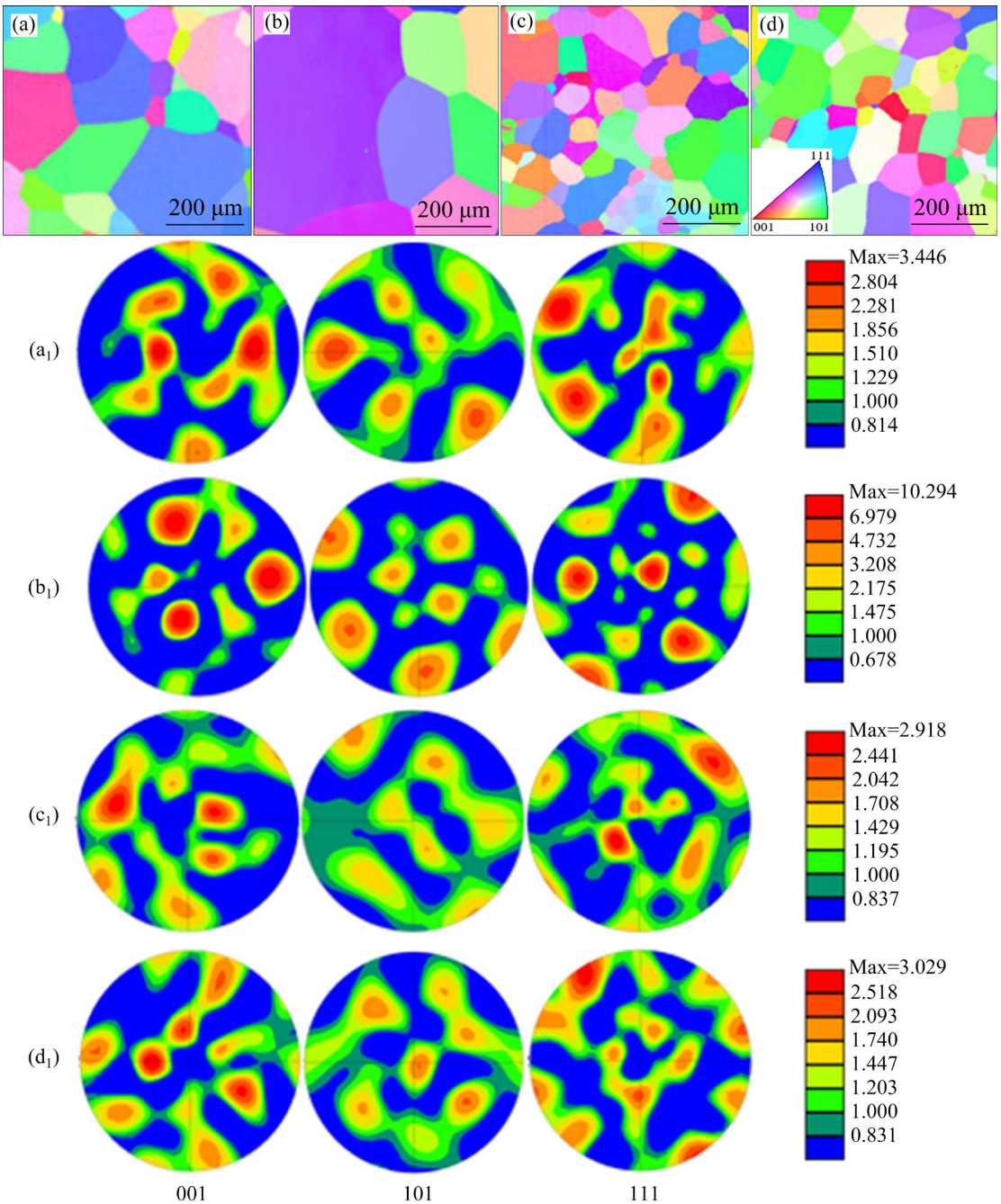

Fig. 13 EBSD images of initial and heat-treated samples: (a, a_1) T5-AC; (b, b_1) T5-5; (c, c_1) T10-AC; (d, d_1) T10-5

T10-AC sample is reduced by 41%. In addition, the phase transition temperature can be much lower than 500 °C, and the crystal structure maintains an initial state with grain coarsening only after a brief aging treatment [42,43]. Meanwhile, the stability of T5 is less than that of T10. The texture of bcc structure in the T5-5 sample is stronger compared to the T5-AC sample. Meanwhile, the maximum pole density is larger than 10.2, resulting in lower hardness and compressive yield strength [34,35]. The lattice distortion effect of crystal structure and sluggish diffusion effect of alloying elements can restrain rapid diffusion of alloying elements during heat treatment at 900 °C. Thus, a large amount of hcp structure is distributed uniformly throughout bcc structure, as shown in Fig. 14(a). The hcp structure is distributed mainly along the grain boundary when a small amount of hcp structure is

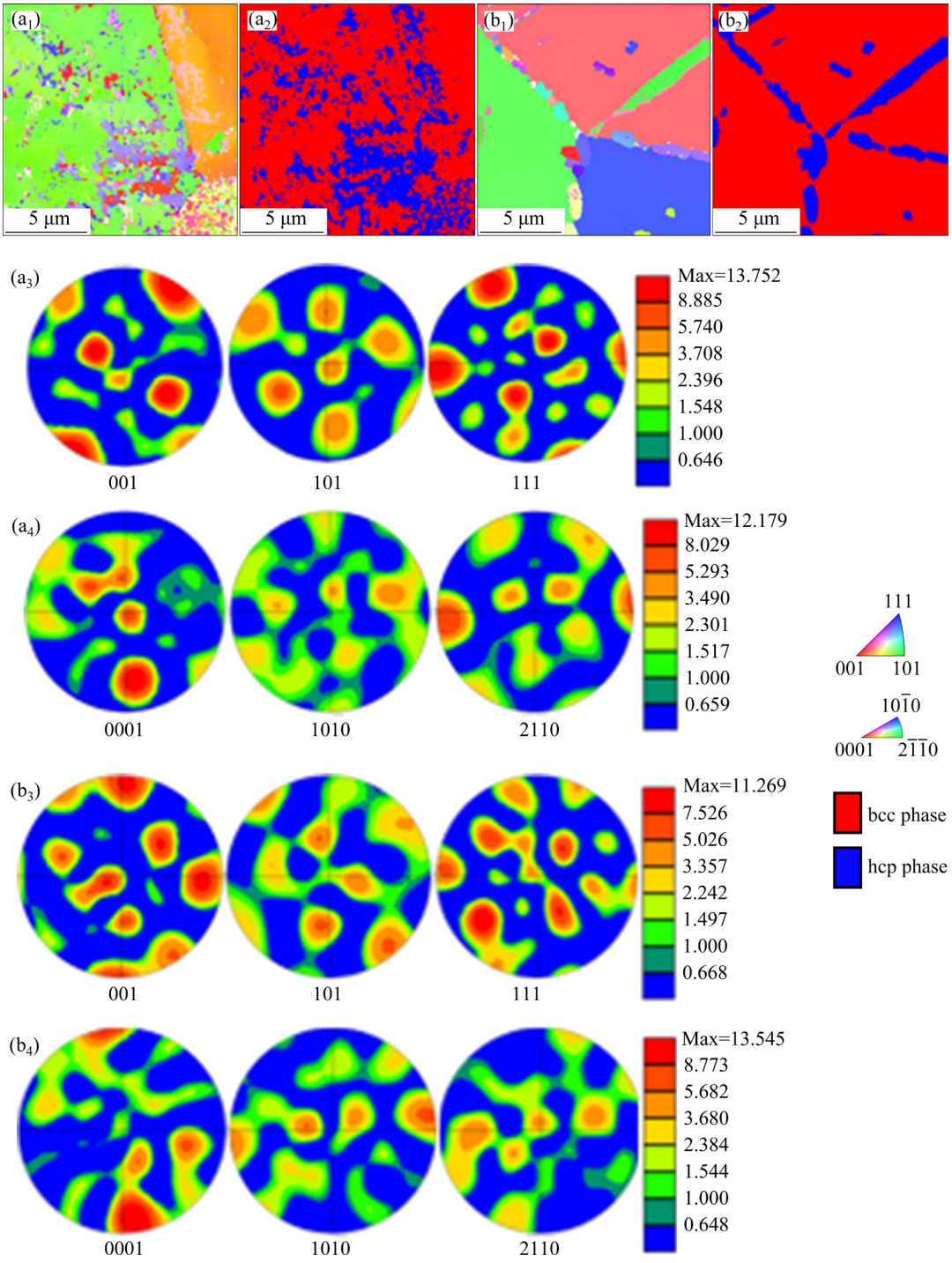

Fig. 14 EBSD images of T5-9 (a_1−a_4) and T10-9 (b_1−b_4) samples: (a_1, b_1) IPF images; (a_2, b_2) Phase morphologies; (a_3, b_3) PF maps of bcc phase; (a_4, b_4) PF maps of hcp phase

discovered near the grain boundary. The area ratio of the hcp phase is decreased from 48% of T5-9 to 6.8% of T10-9. Simultaneously, stronger textures of the hcp and bcc structures are detected in Figs. 14(a_3, a_4, b_3, b_4). For this reason, the stronger texture may contribute to the anisotropy of mechanical properties, and the quantity of slip systems in the hcp structure is less than that in the bcc structure [44]. For Ti-containing high-entropy alloy, a shear band can be formed easily at the (0001) crystallographic plane, resulting in the fracture in the direction of 45° along deformation direction [45,46], as shown in Fig. 11(b_2). In a word, increased hardness and reduced fracture strain can both be attributed to a uniform hcp structure. These results are in agreement with the results of Refs. [47−49]. And the precipitation strengthening and deformation- induced strengthening can contribute to a higher yield strength [50,51]. But hcp structure can be formed when Al is increased to above 15 at.%, thus resulting in tremendous embrittlement and low malleability [52].

4 Conclusions

(1) The phase of as-cast samples with increasing Cr, Al, and Mn element contents is transformed from a single phase with bcc structure to dual phases with hcp structure.

(2) Higher oxidation mass gain rate occurs with low-content alloying elements of Cr, Al, and Mn. A continuously protective oxidation layer of $(Al,Cr)_2O_3$ or Cr−O oxides contributes to excellent oxidation resistance.

(3) There is a growing tendency in micro-hardness before/after heat treatment with increasing Al, Cr, and Mn element contents. Lower micro-hardness can be ascribed to the coarse grain size. But dual phases with hcp structure are precipitated to enhance microhardness after heat treatment at 900 °C.

(4) The yield strength of the initial samples is gradually increased with increasing the element contents according to assumed linear relationship. The yield strengths of T5-AC, T10-AC, T15-AC and T20-AC samples are 888.8, 1260.3, 1618.8, and 1989.4 MPa, respectively. After heat treatment at 900 °C, the deformation-induced strengthening also contributes to increasing the compressive strength by sacrificing its malleability.

CRediT authorship contribution statement

Ping-hu CHEN: Conceptualization, Methodology, Formal analysis, Investigation, Writing − Review & editing, Visualization, Funding acquisition, Project administration, Resources; **Bai-chun LI:** Investigation, Writing − Original draft, Data curation; **Zhen LIU:** Investigation, Data curation; **Ying-hao ZHOU:** Investigation, Writing − Review & editing; **Rui-qing LI:** Investigation, Writing − Review & editing, Funding acquisition; **Yun ZHANG:** Investigation, Writing − Review & editing, Methodology, Visualization, Funding acquisition, Supervision, Resources.

Declaration of competing interest

The authors declare that they have no known competing financial interests or personal relationships that could have appeared to influence the work reported in this paper.

Acknowledgments

This work was funded by Open Research Fund of State Key Laboratory of Precision Manufacturing for Extreme Service Performance, Central South University, China (No. Kfkt2020-01), Hunan Provincial Natural Science Foundation, China (No. 2021JJ40774) and the Project of State Key Laboratory of High Performance Complex Manufacturing, Central South University, China (No. ZZYJKT2021-01).

References

[1] GUPTA A, KHATIRKAR R, SINGH J. A review of microstructure and texture evolution during plastic deformation and heat treatment of β-Ti alloys [J]. Journal of Alloys and Compounds, 2022, 899: 163242.

[2] CASADEBAIGT A, HUGUES J, MONCEAU D. High temperature oxidation and embrittlement at 500−600 °C of Ti−6Al−4V alloy fabricated by laser and electron beam melting [J]. Corrosion Science, 2020, 175: 108875.

[3] LI Guang-xian, CHANDRA S, RASHID R, PALANISAMY S, DING Song-lin. Machinability of additively manufactured titanium alloys: A comprehensive review [J]. Journal of Manufacturing Processes, 2022, 75: 72−99.

[4] WANG Qi-peng, KONG Jian, LIU Xiang-kui, DONG Ke-wei, SONG Xin-xiang, YANG Yang, XU Jun-qiang, CHEN Xin-sheng. The effect of a novel low-temperature vacuum heat treatment on the microstructure and properties of Ti−6Al−4V alloys manufactured by selective laser melting [J]. Vacuum, 2021, 193: 110554.

[5] SUI Shang, CHEW You-xiang, HAO Zhi-wei, WENG Fei, TAN Chao-lin, DU Zheng-lin, BI Gui-jun. Effect of cyclic heat treatment on the microstructure and mechanical

properties of laser aided additive manufacturing Ti−6Al−2Sn−4Zr−2Mo alloy [J]. Advanced Powder Materials, 2022, 1(1): 100002.

[6] GHOSH A, SAHU V K, GURAO N P. Effect of heat treatment on the ratcheting behaviour of additively manufactured and thermo-mechanically treated Ti−6Al−4V alloy [J]. Materials Science and Engineering A, 2022, 833: 142345.

[7] HE Dong-sheng, LI Liu-he, GUO Wei, HE Guang-zhi, PENG Peng, SHAO Tian-wei, HUAN Heng, ZHANG Gong-xuan, HAN Guo-feng, YAN Jian-feng. Improvement in oxidation resistance of Ti_2AlNb alloys at high temperatures by laser shock peening [J]. Corrosion Science, 2021, 184: 109364.

[8] LI Shen, YAMAGUCHI T. High-temperature oxidation performance of laser-cladded amorphous TiNiSiCrCoAl high-entropy alloy coating on Ti−6Al−4V surface [J]. Surface and Coatings Technology, 2022, 433: 128123.

[9] LU Yao-ping, QU De-yi, DUAN Yong-hua, PENG Ming-jun. Microstructure and high-temperature oxidation behaviors of surface layer on TA2 pure titanium by boriding and aluminizing two-steps method [J]. Ceramics International, 2022, 48(4): 5646−5654.

[10] XU Duo, LU Zhi-yuan, WANG Tian-yu, WANG Shu-dan, JIANG Yao, XU Zheng-yu, BI Zheng-gang, GENG Shuo. Novel Ti-based alloys prepared with different heat treatment strategies as antibacterial biomedical implants [J]. Materials & Design, 2021, 205: 109756.

[11] LI Shu-han, LAN Xin-qiang, WANG Ze-min, MEI Shu-wen. Microstructure and mechanical properties of Ti−6.5Al−2Zr−Mo−V alloy processed by laser powder bed fusion and subsequent heat treatments [J]. Additive Manufacturing, 2021, 48(Part A): 102382.

[12] YIM S, BIAN Hua-kang, AOYAGI K, CHIBA A. Effect of multi-stage heat treatment on mechanical properties and microstructure transformation of Ti−48Al−2Cr−2Nb alloy [J]. Materials Science and Engineering A, 2021, 816: 141321.

[13] YANG W, PARK J, CHOI K, CHUNG C H, LEE J, ZHU Jun, ZHANG Fan, PARK J S. Evaluation of growth kinetics of aluminide coating layers on Ti−6Al−4V alloys by pack cementation and the oxidation behaviours of the coated Ti−6Al−4V alloys [J]. International Journal of Refractory Metals and Hard Materials, 2021, 101: 105642.

[14] JIN Ke, BEI Hong-bin. Physical properties of high entropy alloys [J]. Encyclopedia of Materials: Metals and Alloys, 2022, 2: 474−483.

[15] FENG Rui, GAO M C, ZHANG Chuan, GUO Wei, POPLAWSKY J D, ZHANG Fan, HAWK J A, NEUEFEIND J C, REN Yang, LIAW P K. Phase stability and transformation in a light-weight high-entropy alloy [J]. Acta Materialia, 2018, 146: 280−293.

[16] ZHANG Yang, AI Yun-long, CHEN Wei-hua, OUYANG Sheng. Preparation and microstructure and properties of AlCuFeMnTiV lightweight high entropy alloy [J]. Journal of Alloys and Compounds, 2022, 900: 163352.

[17] KNAISLOVÁ A, NOVÁK P, PRŮŠA F, CABIBBO M, JAWORSKA L, VOJTĚCH D. High-temperature oxidation of Ti−Al−Si alloys prepared by powder metallurgy [J]. Journal of Alloys and Compounds, 2019, 810: 151895.

[18] JIANG Hui-ren, WANG Zhong-lei, MA Wen-shuai, FENG Xiao-ran, DONG Zi-qiang, ZHANG Liang, LIU Yong. Effects of Nb and Si on high temperature oxidation of TiAl [J]. Transactions of Nonferrous Metals Society of China, 2008, 18(3): 512−517.

[19] TIAN H, ZHOU K, ZOU Y C, CAI H, WANG Y M, OUYANG J H, LI X W. Microstructure and high temperature oxidation resistance property of packing Al cementation on Ti−Al−Zr alloy [J]. Surface and Coatings Technology, 2019, 374: 1051−1058.

[20] PENG Bin, LI Hai-qing, ZHANG Quan, XU Yu-X, WEI Tie-feng, WANG Qi-min, ZHANG Feng-ge, KIM Kwang-ho. High-temperature thermal stability and oxidation resistance of Cr and Ta co-alloyed Ti−Al−N coatings deposited by cathodic arc evaporation [J]. Corrosion Science, 2020, 167: 108490.

[21] JIANG Bei-bei, WEN Dong-hui, WANG Qing, CHE Jin-da, DONG Chuang, LIAW P K, XU Fen, SUN Li-xin. Design of near-α Ti alloys via a cluster formula approach and their high-temperature oxidation resistance [J]. Journal of Materials Science & Technology, 2019, 35(6): 1008−1016.

[22] DAI Jing-jie, LI Shou-ying, ZHANG Hong-xia, YU Hui-jun, CHEN Chuan-zhong, LI Yang. Microstructure and high-temperature oxidation resistance of Ti−Al−Nb coatings on a Ti−6Al−4V alloy fabricated by laser surface alloying [J]. Surface and Coatings Technology, 2018, 344: 479−488.

[23] HE Jia-hua, GUO Xi-ping, QIAO Yan-qiang. Oxidation and hot corrosion behaviors of Nb−Si based ultrahigh temperature alloys at 900 °C [J]. Transactions of Nonferrous Metals Society of China, 2021, 31(1): 207−221.

[24] CAO Yuan-kui, LIU Yong, LIU Bin, ZHANG Wei-dong, WANG Jia-wen, DU Meng. Effects of Al and Mo on high temperature oxidation behavior of refractory high entropy alloys [J]. Transactions of Nonferrous Metals Society of China, 2019, 29(7): 1476−1483.

[25] LIU Hai-yong, FENG Ya-jie, LI Peng, SHI Xiao-guang, ZHU Han, SHU Jie, HUANG Qing, GE Fang-fang, HUANG Feng. Enhanced plasticity of the oxide scales by in-situ formed Cr_2O_3/Cr heterostructures for Cr-based coatings on Zr alloy in 1200 °C steam [J]. Corrosion Science, 2021, 184: 109361.

[26] ZHOU Chuan-gen, YANG Ying, GONG Sheng-kai, XU Hui-bin. Effect of Ti−Al−Cr coatings on the high temperature oxidation behavior of TiAl alloys [J]. Materials Science and Engineering A, 2001, 307: 182−187.

[27] SWADŹBA R, BAUER P P. Microstructure formation and high temperature oxidation behavior of Ti−Al−Cr−Y−Si coatings on TiAl [J]. Applied Surface Science, 2021, 562: 150191.

[28] LASKA N, BRAUN R, KNITTEL S. Oxidation behavior of protective Ti−Al−Cr based coatings applied on the γ-TiAl alloys Ti-48-2-2 and TNM-B1 [J]. Surface and Coatings Technology, 2018, 349: 347−356.

[29] BRODNIKOVSKII N P, ORYSHICH I V, PORYADCHENKO N E, KUZNETSOVA T L, KHMELYUK N D,

ROKITSKAYA E A. Resistance of titanium−chromium and zirconium−chromium alloys to air oxidation [J]. Powder Metallurgy and Metal Ceramics, 2010, 49(7/8): 454−459.

[30] SAMIMI P, LIU Yue, GHAMARIAN I, BRICE D A, COLLINS P C. A new combinatorial approach to assess the influence of alloy composition on the oxidation behavior and concurrent oxygen-induced phase transformations for binary Ti−*x*Cr alloys at 650 °C [J]. Corrosion Science, 2015, 97: 150−160.

[31] SONG H J, LEE H W, LEE J Y, MOON W J, LEE W Y, PARK Y J. Characteristics and oxidation mechanism of thermal oxide on Ti−*x*Cr and Ti−*x*V (*x*=5, 10, 15) alloys [J]. Journal of Alloys and Compounds, 2020, 815: 152390.

[32] ZENG Xian, LIU Zi-yong, WU Gang-gang, TONG Xu, XIONG Ya-qiong, CHENG Xu-dong, WANG Xuan-guo, YAMAGUCHI T. Microstructure and high- temperature properties of laser cladded AlCoCrFeNiTi0.5 high-entropy coating on Ti 6Al−4V alloy [J]. Surface and Coatings Technology, 2021, 418: 127243.

[33] DAI Jing-jie, ZHANG Nian-long, WANG A-min, ZHANG Hong-xia, CHEN Chuan-zhong. Microstructure and high temperature oxidation behavior of Ti−Al−Nb−Si coatings on Ti−6Al−4V alloy [J]. Journal of Alloys and Compounds, 2018, 765: 46−57.

[34] TONG Zhao-peng, REN Xu-dong, JIAO Jia-fei, ZHOU Wang-fan, REN Yun-peng, YE Yun-xia, LARSON E A, GU Jia-yang. Laser additive manufacturing of FeCrCoMnNi high-entropy alloy: Effect of heat treatment on microstructure, residual stress and mechanical property [J]. Journal of Alloys and Compounds, 2019, 785: 1144−1159.

[35] LIU Wei, TU Hai-ling, GAO Ming, SU Xiao-ping, ZHANG Shu-yu, HUO Cheng-song, YANG Hai. High performance DLC/BP and ZnS/YbF_3 double-layer protective and antireflective coatings [J]. Journal of Alloys and Compounds, 2013, 581: 526−529.

[36] RAHULAN N, SHARMA S S, RAKESH N, SAMBHU R. A short review on mechanical properties of SLM titanium alloys based on recent research works [J]. Materials Today: Proceedings, 2022, 56(Part 5): 7−12.

[37] AWAD A H, EL-HOFY H A, CHIBA A, GEPREEL M. Robust mechanical properties and corrosion resistance of new low-cost hot-forged and aged β-type Ti−14Mn−(*x*)Zr alloys [J]. Journal of Alloys and Compounds, 2022, 904: 164098.

[38] JAWED S F, RABADIA C D, LIU Y J, WANG L Q, LI Y H, ZHANG X H, ZHANG L C. Beta-type Ti−Nb−Zr−Cr alloys with large plasticity and significant strain hardening [J]. Materials & Design, 2019, 181: 108064.

[39] SHAH F A, TROBOS M, THOMSEN P, PALMQUIST A. Commercially pure titanium (cp-Ti) versus titanium alloy (Ti6Al4V) materials as bone anchored implants—Is one truly better than the other? [J]. Materials Science and Engineering C, 2016, 62: 960−966.

[40] PUSHP P, DASHARATH S M, ARATI C. Classification and applications of titanium and its alloys [J]. Materials Today: Proceedings, 2022, 54(Part 2): 537−542.

[41] ZHANG Guo-hong, CHAE Jae-yong, KIM Kwan-ho, SUH Dong-woo. Effects of Mn, Si and Cr addition on the dissolution and coarsening of pearlitic cementite during intercritical austenitization in Fe-1mass.%C alloy [J]. Materials Characterization, 2013, 81: 56−67.

[42] YUMAK N, ASLANTAŞ K. A review on heat treatment efficiency in metastable β titanium alloys: The role of treatment process and parameters [J]. Journal of Materials Research and Technology, 2020, 9(6): 15360−15380.

[43] SANTHOSH R, GEETHA M, SAXENA V K, NAGESWARARAO M. Studies on single and duplex aging of metastable beta titanium alloy Ti−15V−3Cr−3Al−3Sn [J]. Journal of Alloys and Compounds, 2014, 605: 222−229.

[44] DING Zhi-gang, LIU Wei, LI Shuang, ZHANG Da-long, ZHAO Yong-hao, LAVERNIA E J, ZHU Yun-tian. Contribution of van der Waals forces to the plasticity of magnesium [J]. Acta Materialia, 2016, 107: 127−132.

[45] LIU Cheng-ze, GUAN Hong, TAI Qing-gan, YUAN Fu-sen, HAN Fu-zhou, GU Heng-fei, ZHANG Li-feng, LI Ge-ping. Microstructure, texture and mechanical studies of an inconspicuous shear band formed during hot compression of Ti−6Al−4V alloy [J]. Materials Science and Engineering A, 2017, 698: 18−26.

[46] ZHENG Chao, WANG Fu-chi, CHENG Xing-wang, LIU Jin-xu, LIU Teng-teng, ZHU Zheng-xin, YANG Kai-wen, PENG Mei-qi, JIN Dan. Capturing of the propagating processes of adiabatic shear band in Ti−6Al−4V alloys under dynamic compression [J]. Materials Science and Engineering A, 2016, 658: 60−67.

[47] XIE Zong-yu, OU Xiao-qin, NI Song, SONG Min. Phase transition and hardness evolution of a Ti−5Al−5Mo−1Fe−1Cr alloy subjected to isothermal aging [J]. Micron, 2019, 116: 15−21.

[48] XIONG Cheng-yang, XUE Peng-fei, SUN Bao-hui, LI Yan. Effect of annealing temperature on the microstructure and superelasticity of Ti−19Zr−10Nb−1Fe alloy [J]. Materials Science and Engineering A, 2017, 688: 464−469.

[49] HE Bei, CHENG Xheng, LI Jia, LI Guo-chao, WANG Hua-ming. ω-assisted α phase and hardness of Ti−5Al−5Mo−5V−1Cr−1Fe during low temperature isothermal heat treatment after laser surface remelting [J]. Journal of Alloys and Compounds, 2017, 708: 1054−1062.

[50] SWITZNER N T, VAN TYNE C J, MATAYA M C. Effect of forging strain rate and deformation temperature on the mechanical properties of warm-worked 304L stainless steel [J]. Journal of Materials Processing Technology, 2010, 210(8): 998−1007.

[51] SHI Xiao-hui, ZENG Wei-dong, ZHAO Qin-yang. The effects of lamellar features on the fracture toughness of Ti-17 titanium alloy [J]. Materials Science and Engineering A, 2015, 636: 543−550.

[52] DELVAT E, GORDIN D M, GLORIANT T, DUVAL J L, NAGEL M D. Microstructure, mechanical properties and cytocompatibility of stable beta Ti−Mo−Ta sintered alloys [J]. Journal of the Mechanical Behavior of Biomedical Materials, 2008, 1(4): 345−351.

热处理过程 TiAlCrMn 高熵合金的高温氧化特性与力学性能

陈平虎[1]，李柏春[2]，刘 震[1]，周英豪[3]，李瑞卿[4]，张 昀[5]

1. 深圳大学 机电与控制工程学院 增材制造所，深圳 518060；
2. 哈尔滨工业大学(深圳) 材料科学与工程学院，深圳 518055；
3. 香港城市大学 机械工程学院，香港；
4. 中南大学 轻合金研究院 高性能复杂制造国家重点实验室，长沙 410083；
5. 湖南科技大学 机电工程学院，湘潭 411201

摘 要：采用真空熔炼制备不同 Al、Cr、Mn 含量的 TiAlCrMn 系高熵合金，并对其高温氧化特性和热处理前后的力学性能进行研究。结果表明，随着 Al、Cr、Mn 含量的增加，其高温氧化质量增加率明显降低，这是因为在氧化层中形成了连续且致密的富(Al,Cr)氧化物，阻碍氧原子与其他合金原子相互扩散形成新的氧化物。另外，热处理前后的样品，其显微硬度均存在单调递增的趋势，晶粒粗化会导致样品硬度降低，而在高含量合金元素的样品中，析出强化会改善其硬度。变形诱导强化使材料获得更高的压缩强度，在 500 ℃热处理后的样品其屈服强度有所降低，而经过 900 ℃热处理的材料屈服强度得到提升，但其延展性降低。

关键词：高熵合金(HEAs)；抗氧化性；显微组织演变；显微硬度；压缩强度

(Edited by Bing YANG)